

The phase-space distribution of present-day lenticular galaxies in relaxed galaxy clusters

Gort Mathias

Department of Quantum Physics and Astrophysics, University of Barcelona

June 28, 2024

ABSTRACT

Aims. In this work we investigate the distribution of lenticular galaxies (S0s) in the projected phase space (PPS) of local, relaxed galaxy clusters. The aim is to shed further light on the still debated formation and evolutionary processes that shape S0s, by probing the properties of different subpopulations of actively star-forming (SF) and passive systems in which the heterogeneous class of lenticular galaxies can be divided.

Methods. Optical and X-ray cluster identifications, along with tests to estimate the degree of virialization and substructure of galaxy associations, are used to select a sample of cluster regions with maximally relaxed cores. A PPS diagram is then constructed for this ensemble of clusters. Subsequently, a series of statistical tests are applied to the S0 member galaxies to compare the phase-space distributions of various S0 subpopulations and their times since cluster infall. Finally, line-of-sight velocity dispersion and specific star-formation rate (SSFR) radial profiles are constructed for both active and passive S0s.

Results. Local, relaxed galaxy clusters contain $\sim 80\%$ of passive S0s and $\sim 20\%$ of star-forming S0s. The PPS distributions of these two classes of S0s are significantly different, with the passive systems concentrated closer to the cluster centers, and the active S0s being more abundant in the outer cluster regions. We find evidence that active S0s have been accreted more recently than passive S0s, with a gap in mean cluster infall time of about 1 Gyr. Despite these differences, the LOS velocity dispersions of these two subpopulations of S0s exhibit surprisingly similar projected radial profiles, consistent with radial infall. However, the SSFR radial profiles differ markedly: passive S0s show a flat profile up to three virial radii, while active lenticulars experience a sharp decline in SSFR between ~ 2.5 and $1.5 R_{\text{vir}}$, followed by a more gradual decrease extending to the cluster center.

Key words. ASTRONOMY AND ASTROPHYSICS – GALAXIES

1. Introduction

Lenticular galaxies (S0s) are the morphological family located at the crossroad between the branches of spiral and elliptical galaxies in the Hubble classification scheme. While sharing multiple physical properties with early-type objects, structurally they resemble more late-type disk galaxies, although their thicker, lenticular disks lack spiral arms. Furthermore, unlike the other morphological types, the population of S0s is abundant in both high and low galactic density regions. This suggests a complex—or possibly multiple—formation and evolutionary pathway(s) for these objects (Wilman & Erwin 2012). The distribution of S0 galaxies in the Local Universe is known to follow the morphology-density relation described by Dressler (1980), where lenticulars, despite their ubiquity, are predominantly found in the densest cosmic regions, such as galaxy groups and the centers of galaxy cluster regions. Consequently, studying present-day galaxy clusters can offer valuable insights into the still relatively poorly understood formation and evolutionary processes that shape S0 galaxies.

In recent years, simulations of galaxy interactions have concluded that S0s can form by minor mergers between disk galaxies and small satellites, or even from major mergers between pairs of gas-rich, star-forming (SF) spirals (Querejeta et al. 2015; Tapia et al. 2017; Eliche-Moral et al.

2018). Additionally, it is widely accepted that lenticulars can also form through hydrodynamical interactions between the galactic interstellar medium (ISM) and the intra-group/intracluster medium (IGM/ICM, respectively) via mechanisms such as ram pressure stripping (RPS) that can deplete the neutral gas content of spiral galaxies when they move at large speeds in these high-density environments (Gunn & Gott 1972; Nulsen 1982). Other transport processes (thermal evaporation and turbulent stripping Nulsen 1982), tidal interactions, galaxy harassment (Moore et al. 1999), and/or strangulation (Larson et al. 1980; Tinsley 1980), can also contribute to the morphological transformation of spiral galaxies into lenticulars in groups and clusters (Solanes & Salvador-Sole 1992; Dressler et al. 1997; Fasano et al. 2000; Quilis et al. 2000; Cowl & Kenney 2008; Poggianti et al. 2009; D’Onofrio et al. 2015). Observational studies, both photometric and spectroscopic, have further supported the idea that S0 galaxies do not follow a single evolutionary pathway. These studies have identified at least two subpopulations within this morphological class, each with significantly different intrinsic properties (Xiao et al. 2016; Fraser-McKelvie et al. 2018; Deeley et al. 2020; Domínguez Sánchez et al. 2020; Coccato et al. 2022; Rathore et al. 2022). A recent investigation by Tous et al. (2020), which analyzed the variance of the optical spectra of 68,043 S0s within $z \leq 0.1$ (i.e. the Local Universe), re-

vealed that this Hubble type encompasses objects with a wide range of SF levels. Using Principal Component Analysis (PCA) on the spectra, the authors found that their projections onto the latent space defined by the first two principal components (PC1 and PC2) fall into two clearly distinct regions containing objects with statistically inconsistent physical properties. Based on these findings, Tous et al. divided the S0s into three subpopulations according to their location in this subspace: the "Passive Sequence" (S0-PS), which results from the strong correlation of the two PCs of the spectra and forms a narrow but densely populated diagonal band comprising approximately 69% of the total sample; the "Active Cloud" (S0-AC), a less crowded, more scattered region adjacent to the PS containing about 25% of all the S0s; and a narrow "Transition Region" (S0-TR) in between, consisting of $\sim 6\%$ of the S0 galaxies with intermediate spectral properties. Overall, the members of the S0-AC population compared to their PS counterparts are less massive, more luminous with less concentrated light profiles, younger, bluer, metal-poorer, and are found to avoid high-density environments. In terms of their optical spectra, S0-PS occupy essentially the same region in the PC1-PC2 subspace as elliptical galaxies, while the area covered by the S0-AC substantially overlaps with the region defined by spiral galaxies in this same diagram. In fact, as we will also show in the present analysis, members of the S0-AC class often exhibit similar levels of SF as late-type galaxies (Kaviraj et al. 2007; Tous et al. 2020), suggesting that, contrary to common assumptions, the S0 local population is not entirely composed of "red and dead objects". These findings about the activity of S0s and their diverse formation paths are supported by recent state-of-the-art hydrodynamic cosmological simulations (e.g. Deeley et al. 2021).

The present master's thesis aims to further investigate the multiple formation pathways of S0 galaxies by analyzing data from galaxy cluster regions in the Local Universe ($z \lesssim 0.1$). These regions include a central, virialized, high-density galaxy association, the proper cluster, that facilitates hydrodynamic interactions, as well as a surrounding secondary infall region populated by galaxy groups where gravitational mechanisms, primarily mergers, are effective at pre-processing galaxies and driving their evolution before they become full cluster members. Inspired by the work of Rhee et al. (2017), we will approach this goal by studying the locations in projected phase space (PPS) coordinates (i.e., line of sight velocities, and projected distances from the cluster center) of actively star-forming and quiescent S0s in $z \sim 0$ cluster regions. We will examine whether there are differences in the phase-space distributions of these activity classes and determine whether we can use these differences, along with the predictive power of the diagram, to glean insights into the environmental effects that may be acting or have acted upon the population of lenticular galaxies and ultimately reveal the physical mechanisms that drive their formation.

The contents of this report are as follows. A description of the data used is given in Section 2. The selection process followed to obtain the final sample of cluster regions and their S0 member galaxies is explained in Section 3. The results are presented in Section 4, followed by a discussion in Section 5. Finally, our conclusions are summarized in Section 6. For all calculations a flat Λ CDM cosmology with $H_0 = 70 \text{ km s}^{-1} \text{ Mpc}^{-1}$ is assumed.

2. Data

Here, we outline the main characteristics of the data catalogs that we use to identify both galaxy cluster regions and S0 galaxies in the Local Universe suitable for this study.

2.1. Galaxy clusters from optical data

Our local galaxy cluster regions have been selected from the group catalog of Tempel et al. (2017). We note that Tempel et al. only speak of "groups", regardless of their mass or number of members, with two being the minimum value of the latter they use to define a group. They provide three catalogs, all based on the twelfth data release of the Sloan Digital Sky Survey (Eisenstein et al. 2011; Alam et al. 2015), hereafter SDSS-DR12. The first catalog consists of all galaxies that were considered in the survey, regardless if they are members of groups or isolated. Only galaxies included in the main contiguous area of the survey with spectroscopic and photometric data and apparent Petrosian r -band magnitude brighter than 17.77 (the Main SDSS Legacy Survey), as well as with $z \leq 0.2$ are included in this catalog. The total number of objects is 584,449. The second catalog lists all groups they identify (see below), while the third dataset collects all galaxy systems that show evidence of merging.

To find groups, Tempel et al. adopt the Friends-of-Friends (FoF) algorithm (Turner & Gott 1976; Beers et al. 1982; Zeldovich et al. 1982; Barnes et al. 1985) with membership refinement procedures. The key parameter of this tool is the linking length, used to identify all pairs of particles with an interparticle separation equal or less than its value. Such pairs are designated friends, and groups are defined as sets of particles that are connected by one or more friendship relations, i.e., friends of friends. An important effect to consider is the dependence of the linking length on redshift. Tempel et al. use an arctan law and find the linking length at redshift $z = 0$ to be 0.34 Mpc. They also distinguished between radial and transversal linking lengths with a ratio of 12 between the two (as suggested by Duarte & Mamon (2014)).

The biggest limitation of the FoF algorithms is their tendency to incorrectly identify merging systems or groups that lie close to each other, as well as field galaxies located near groups, as single, larger systems. To prevent this, Tempel et al. refined the group membership process in two steps. First, by splitting multiple components of groups into separate systems aided by multimodality analysis. And second, by using estimates of the virial radius and escape velocity of the groups¹ to exclude those galaxies that are not physically bound to the systems. The exclusion of galaxies from groups was carried out iteratively. They also identified in their catalog potentially, not necessarily real, merging systems when the intercentric distance of two groups in the sky plane was smaller than the sum of their radii.

In the contiguous area of the Legacy Survey, Tempel et al. identified 88,662 galaxy groups with at least two members, including 498 merging systems. As for the galaxies, 49% belong to one of the detected groups. Tempel et al.'s

¹ For this they assume a Navarro, Frenk & White (NFW) dark matter density profile (Navarro et al. 1995) and use R_{200} , the radius of the spherical region around the cluster center within which the mean cluster density exceeds the average density of the Universe by a factor of 200, as the virial radius.

data also show that richer groups are absent at greater distances, due to flux limitations. However, the maximum number of group members is roughly constant up to $z \simeq 0.1$. This guarantees a uniform sampling of galaxy cluster regions for the purpose of this work.

2.2. X-ray galaxy clusters

The presence of strong and extended X-ray emission in galaxy clusters is a clear indication of a hot ICM and, therefore, signifies that the central regions of these galaxy systems are relaxed and virialized. In the most evolved clusters, it is expected that the peak of X-ray emission is not associated with individual galaxies, except possibly with a central dominant object at the cluster center, the brightest cluster galaxy (BCG), as well as to show little to no offset from the center of mass of the entire system. To ensure that the clusters we select are dynamically evolved structures, we have combined two catalogs of X-ray selected galaxy clusters with the optical cluster data from the previous section.

The two catalogs considered are from the X-Class survey (Koulouridis, E. et al. 2021) and the ROSAT All-Sky Survey (RXGCC) (Xu, Weiwei et al. 2022). The X-Class cluster catalog includes a total 1,646 systems with redshifts up to $z = 1.5$, and their redshift distribution peaking at $z = 0.1$. However, only 297 clusters ($\sim 19\%$ of the total), meet the criterion of being located in the Local Universe. In contrast, the RXGCC catalog contains a total of 944 X-ray clusters, of which 619 (66%) lie within our redshift limit of $z \leq 0.1$. The total number of X-ray clusters retrieved from both catalogs is therefore 916. However, this number may include duplicate galaxy systems, as the two X-ray surveys cover similar regions in the sky. To account for this, the two catalogs were crossmatched by comparing the sky coordinates of their X-ray centers and their measured redshifts, allowing for maximum uncertainties of 3 arcmin in the coordinates (a small fraction of the degree-sized spatial extensions of these galaxy systems on the sky) and 0.005 in the redshift (equivalent to the mean redshift error from the RXGCC catalog). We found 120 clusters in common, which were then removed from the X-Class catalog and included only from the RXGCC data (due to the larger contribution of this catalog) in the final X-ray cluster sample, which has been constructed by stacking the two catalogs, and results in a total of 796 unique X-ray clusters.

2.3. Lenticular galaxies

The source of present-day lenticulars is the catalog compiled by Tous et al. (2020), which includes a total of 68,043 S0 galaxies. This dataset provides information about their location, redshift, and spectral class (PS/TR/AC), along with a comprehensive list of other properties retrieved from the literature. To determine the lenticular morphology of these galaxies, Tous et al. (2020) used the catalog by Domínguez Sánchez et al. (2018), which provides the T -type values of galaxies in the Main SDSS Legacy Survey, inferred using machine learning techniques.

3. Identification of dynamically evolved cluster regions and their galaxy members

To investigate the distribution of S0 galaxies in the PPS of cluster regions, it is fundamental to select galaxy associations that are fully evolved, ensuring that the positions of the galaxies in the PPS can be interpreted correctly. In this section, we describe the steps taken to obtain a final sample of galaxy clusters that show no obvious signs of being dynamically disturbed, along with their galaxy members.

3.1. Selection of a sample of relaxed cluster regions

To begin, we applied the following filters to the groups catalog by Tempel et al. described in Section 2.1:

- The group redshift z_{clu} can not exceed 0.1, ensuring that it is located in the Local Universe.
- The group mass must be larger than $10^{14} M_{\odot}$, selecting only true galaxy clusters.
- The group radius cannot be larger than 5 Mpc, eliminating unrealistically large galaxy systems.
- The minimum number of galaxy members within the innermost Mpc radius of the group has to be at least 20, ensuring reasonable statistics.
- The group must not be listed in the third catalog of Tempel et al. containing potentially merging systems.

These criteria are verified from the data listed in Tempel et al.'s catalog, where they use R_{200} to represent the radius of the central cluster region and M_{200} for its associated total mass. It is important to note that although these parameters are typically used as proxies, respectively, for the virial radius and mass of clusters, they may underestimate their true values, as the density contrast of galaxy clusters in a standard flat Λ CDM cosmology is actually close to 100 (see, e.g., Darriba & Solanes 2010). For this reason, more accurate estimates of these parameters will be derived in the next section. We also note that Tempel et al. assumed this same cosmology, but with $H_0 = 67.8 \text{ km s}^{-1} \text{ Mpc}^{-1}$. In this case, however, such a minor inconsistency has been ignored throughout the present study.

A final refinement of the sample of relaxed cluster regions is conducted by crossmatching the surviving clusters from Tempel et al. with our selection from the RXGCC and X-Class catalogs (see Sec. 2.2). For this, we employed the same strategy used for the crossmatching of the two X-ray catalogs, comparing the sky coordinates and redshifts of the cluster centers with absolute errors of 3 arcmin in the coordinates and 0.005 in the redshift.

After applying this last filter, we identified a total of 37 relaxed galaxy cluster regions suitable for conducting the present study.

3.2. Refinement of cluster properties

Investigating the PPS of cluster regions requires a thorough identification of their galaxy members. It is important to note that clusters often grow by accreting groups of galaxies rather than single objects (Berrier et al. 2009; McGee et al. 2009). Consequently, all galaxies located at the outskirts of clusters should be considered part of the same cluster region, even if they belong to smaller groups that are being accreted by the central aggregation. Since

each galaxy in Tempel et al.'s catalog is assigned to only one group, some galaxies lying in the secondary infall region might not be counted as members of a cluster region despite actually being part of it. This potential overlook of member galaxies therefore needs to be corrected when defining galaxy membership for our final sample of cluster regions, since the validity of our results relies on the inclusion of *all* galaxies that inhabit the outskirts of clusters, regardless of whether they are part of small infalling groups. This has led us to ignore Tempel et al.'s original classification and reformulate the membership assignment on our own.

To achieve this goal we apply a recursive method using as initial values the central coordinates, redshifts, and velocity dispersions listed in the Tempel et al.'s group catalog. First, an initial estimate of the mean redshift of each cluster region z_{clu} is calculated, by averaging the redshifts of all galaxy members defined by Tempel et al. within a projected radius of 1 Mpc from the center. Next, we apply a $\pm 4\sigma$ -clipping technique to remove any possible contamination of foreground or background galaxies. The galaxies that keep their status of cluster members are then used to re-estimate the central coordinates and redshift of the cluster regions, using the robust biweight estimator for location from Beers et al. (1990):

$$C_{BI} = M + \frac{\sum_{|u_i| < 1} (x_i - M)(1 - u_i^2)^2}{\sum_{|u_i| < 1} (1 - u_i^2)^2}, \quad (1)$$

where M is the sample median, x_i are the sample elements, and the u_i values are inferred from the expression

$$u_i = \frac{x_i - M}{k \cdot MAD}. \quad (2)$$

In the last equation, we choose $k = 6$ to achieve the best efficiency for location estimation, with data up to four standard deviations from the central location (Mosteller & Tukey 1977), while $MAD = \text{median}(|x_i - M|)$ is the median absolute deviation from the sample median M . Beers et al. (1990) also provide a robust estimator of scale

$$S_{BI} = \sqrt{n} \frac{\left[\sum_{|u_i| < 1} (x_i - M)^2 (1 - u_i^2)^4 \right]^{1/2}}{\left| \sum_{|u_i| < 1} (1 - u_i^2)(1 - 5u_i^2) \right|}, \quad (3)$$

which is used to calculate the cluster velocity dispersion, σ_{clu} .

All these estimators are further refined by recalculating their values until convergence, typically achieved after only a few iterations (in our case three). It is important to note that although these calculations are based on galaxy members within 1 Mpc of the cluster centers, the values obtained from these inner region should be representative of the entire galaxy cluster and, particularly, of its central most virialized region.

To estimate the virial radius R_{vir} the following equation is used:

$$R_{\text{vir}} = \sqrt{3} \sigma_{\text{clu}} \left[\frac{\Omega_M \Delta_{\text{vir}}(z_{\text{clu}})}{200} \right]^{1/2} (1 + z_{\text{clu}})^{-3/2}, \quad (4)$$

with the matter density parameter $\Omega_M = 0.3$ and the virial overdensity $\Delta_{\text{vir}} \simeq 337$ at $z \sim 0$ (Bryan & Norman 1998) for the adopted cosmology. The virial mass M_{vir} is then simply given by:

$$M_{\text{vir}} = \frac{4\pi}{3} R_{\text{vir}}^3 100 \rho_{\text{crit}}, \quad (5)$$

with the critical density $\rho_{\text{crit}} = 1.39 \cdot 10^{11} \text{ M}_{\odot} \text{ Mpc}^{-3}$. Finally, the outermost radius for all cluster regions to which galaxies are included is set to $3 R_{\text{vir}}$. The main properties of the final, most relaxed galaxy clusters are listed in Table 1.

3.3. Refinement of galaxy membership using caustics

To go one step further when defining the criteria of cluster membership for galaxies, the caustic lines for the cluster PPS are calculated. This approach restricts the number of galaxies identified as cluster members by applying physical boundaries that correspond to the clusters' escape velocity, which is calculated from the total mass at each radius. In the projected two-dimensional case, this causes the cluster phase-space to form a so-called trumpet shape. In this method, only galaxies lying inside the caustics —meaning galaxies whose LOS velocities are lower than the escape velocity at their projected clustercentric distance— are selected as cluster members. A nice feature of this procedure is that the caustic boundaries can be determined up to several virial radii from the cluster center, since their calculation does not rely on the dynamical state of the system, but only on the total interior mass. The only assumption of the methodology is spherical symmetry, which may not be granted for a single system (especially at large radii), as clusters often appear elongated in one direction of the sky. However, for this study we are going to work with a single system formed by stacking all the clusters included in the final sample, so the caustic lines will be calculated for the whole ensemble of clusters. This will ensure spherical symmetry, due to the random orientation of the clusters in the stacking. The construction of a cluster ensemble is also necessary for conducting sensitive statistical tests and obtaining reliable results for the properties of interest of the different spectral classes of S0s, since the number of these objects in most individual clusters is usually too low. For the stacking, projected clustercentric distances are normalized by their corresponding cluster virial radius, and the LOS velocities by their corresponding cluster velocity dispersion. The caustics are then calculated for the stacked cluster, by following the technique of Diaferio & Geller (1997), where the escape velocity at each projected radius r_{\perp} is calculated by:

$$v_{\text{esc}}(r_{\perp}) = \pm \left\{ -2\Phi(r) \frac{1 - \beta(r)}{3 - 2\beta(r)} \right\}_{r=r_{\perp}}^{\frac{1}{2}}. \quad (6)$$

In eq. (6), $\Phi(r)$ is the gravitational potential profile, which is corrected by a function depending on the velocity anisotropy profile $\beta(r)$. Cluster simulations show, that galaxy motions in cluster centers are mainly random, implying isotropy and therefore $\beta(0) \sim 0$, while near the virial radius, motions become anisotropic, causing β to increase. A good fit to the average anisotropy profile of cluster-mass

cosmological halos is provided by the model of Tiret et al. (2007):

$$\beta(r) = \beta_\infty \frac{r}{r + r_{-2}}, \quad (7)$$

with $\beta_\infty = 0.5$ and r_{-2} the radius of slope -2 in the mass density profile. For a NFW density profile r_{-2} coincides with the profile scale length r_s (see below) and is related to the virial radius and the concentration parameter C , by $C = R_{\text{vir}}/r_s$. For the calculation of the caustics of the cluster ensemble, we will assume $C = 6$, a value characteristic of clusters with total masses of the order of a few $10^{14} M_\odot$ (Macciò et al. (2008), see Sec. 4.1).

The last missing ingredient to obtain the caustic lines is the gravitational potential $\Phi(r)$, which for a NFW dark matter density profile is given by

$$\rho(r) = \frac{\rho_s}{r/r_s(1 + r/r_s)^2}, \quad (8)$$

and

$$\rho_s = \frac{C^3}{3} \left[\ln(1 + C) - \frac{C}{1 + C} \right]^{-1} \bar{\rho}_{\text{clu}}, \quad (9)$$

with $\bar{\rho}_{\text{clu}} \sim 100\rho_{\text{crit}}$.

The integral of the density profile in eq. (8) yields the total halo mass, which with the aid of Poisson's equation can then be used to derive the gravitational potential:

$$\Phi(r) = \frac{4\pi G \rho_s r_s^3}{r} \ln \left(1 + \frac{r}{r_s} \right). \quad (10)$$

As stated above, we will focus on galaxies located within the caustic lines up to $3R_{\text{vir}}$. Thus, our cluster samples encompass a comprehensive representation of the extended region beyond the virialization sphere, where galaxies are infalling towards the cluster core with a non-zero mean radial velocity².

3.4. Identification of the brightest cluster galaxies

In fully virialized clusters, the brightest cluster galaxies (BCGs)³ are expected to occupy a prominent position near the peak of X-ray emission, which in turn typically coincides with the center of the clusters' gravitational potential well. When this alignment is absent, it can indicate incomplete relaxation, often also evidenced by the presence of substructure in the core region.

To ascertain the presence of a truly dominant galaxy within the clusters included in our final sample, we have calculated the differences in absolute r -band magnitudes between the first and second brightest galaxies, $\Delta\mathcal{M}_{2-1}$,

² A recent study based on a large set of IllustrisTNG clusters with $M_{200} > 10^{14} M_\odot$ and $0.01 \leq z \leq 1.0$ by Pizzardo et al. (2024) has determined that the turnaround radius of galaxy clusters, defined as the clustercentric distance where galaxies depart from the Hubble flow, has a typical z -independent value of $4.8 R_{200}$.

³ BCGs are the cluster galaxies ranked highest in terms of luminosity.

and between the second and third ones, $\Delta\mathcal{M}_{3-2}$, located within $1R_{\text{vir}}$. Using these magnitude gaps, we categorize our clusters into single-BCG systems, when a distinct dominant galaxy with $\Delta\mathcal{M}_{2-1} > 0.45$ is identified (i.e., when the BCG is at least 50% brighter than the second ranked galaxy). On the other hand, double-BCG clusters are those for which $\Delta\mathcal{M}_{2-1} < 0.45$ and $\Delta\mathcal{M}_{3-2} \geq 0.45$, indicating the presence of a pair of bright galaxies that stand out from the rest of the cluster members. The remaining clusters for which both $\Delta\mathcal{M}_{2-1}$ and $\Delta\mathcal{M}_{3-2}$ are less than 0.45 are considered non-BCG clusters, as they lack a truly dominant object. These latter systems typically exhibit lower levels of virialization compared to double- or single-BCG clusters. However, we have not excluded them from our analysis, provided they pass the tests for virialization and substructure—which we describe in the next two sections—in order to select the most dynamically relaxed clusters for our study. The BCG magnitudes, luminosity gaps, velocities, and their distances to the center of the galaxy distributions and peak X-ray emissions, as well as the BCG status of the final sample of most relaxed clusters are listed in Table 2.

3.5. Test of virialization

Unrelaxed systems often exhibit discrepancies among the various indicators used to determine their center of mass, including the overall distribution of galaxy members, the peak of X-ray emission, and the sky coordinates and recession velocity of the BCG. The indicator test from Gebhardt & Beers (1991) focuses on verifying if the velocity of the BCG matches the velocity distribution of the clusters member galaxies. The brightest of the galaxies is used instead of the center of X-ray emission because the ICM gas is collisional and therefore relaxes faster than the galaxies. This test in particular estimates the probability of drawing the observed BCG velocity from the distribution of LOS velocities of the cluster members in the cluster rest frame, which are given by

$$v_{\text{los},i} = c \frac{z_i - z_{\text{clu}}}{1 + z_{\text{clu}}}. \quad (11)$$

The "Z-score" for the BCG is then calculated from the equation

$$Z = \frac{v_{\text{BCG}} - v_{\text{clu}}}{\sigma_{\text{clu}}}, \quad (12)$$

with v_{BCG} being the BCG LOS velocity in the cluster rest frame and $v_{\text{clu}} = cz_{\text{clu}}$.

To test if a BCGs velocity is consistent within the velocity distribution of its host cluster, confidence intervals of the Z-score are calculated by using bootstrap resampling. In this work we conduct 10,000 resamplings for each BCG and consider an offset of the BCG velocity significant when the 90% confidence interval⁴ does not bracket zero. The results of the indicator test (Z-score and its confidence interval) for the clusters that pass both this test and the substructure test (described in the next section) are shown in Table 3. In this table, cluster 2236 is listed twice, as 2236A and 2236B. The reason is that this cluster harbors two essentially equally dominant BCGs (see Table 2), so we require them both to pass the indicator test, which they do.

⁴ A 90% confidence interval is chosen for consistency with the test of substructure in Sec. 3.6.

3.6. Test of substructure

A common tool used in the literature for the detection of substructure in clusters and, therefore, with the potential of being predictive in terms of the dynamical state of a cluster is the Dressler-Shectman (DS) test (Dressler & Shectman 1988). Having substructure means, that clusters can be split into multiple subunits according to the positions and velocities of their member galaxies. Only galaxies lying within $1 R_{\text{vir}}$ are considered for this test, as only the cluster cores are expected to be in approximate dynamical equilibrium.

To estimate the substructure within a cluster, the spatial and velocity information of each member galaxy is taken into account. With this data we compute the Δ statistic

$$\Delta = \sum_{i=1}^{N_{\text{gal}}} \delta_i = \sum_{i=1}^{N_{\text{gal}}} \sqrt{\frac{11}{\sigma_{\text{clu}}^2} [(v_{\text{los},i} - v_{\text{clu}})^2 + (\sigma_{\text{nn},i} - \sigma_{\text{clu}})^2]}, \quad (13)$$

where the δ_i are local estimates of the degree of substructure for each galaxy, with $v_{\text{los},i}$ the LOS velocity of each galaxy, and $\sigma_{\text{nn},i}$ the local velocity dispersion inferred from its 10 nearest neighbors, resulting in the factor 11 in front of the equation, which is the standard choice for the DS test. For studies that use a different value of neighbors see, e.g., Pinkney et al. (1996).

To determine the actual degree of substructure, the computed Δ value is compared with the distribution of values of the same parameter that one obtains in a number of Monte Carlo randomizations (Halliday et al. 2004; Rumbaugh et al. 2013) of the cluster data, by shuffling the galaxy velocities while maintaining their spatial distribution. A large value of δ_i for a given galaxy implies a high probability for it to be located in a spatially compact subsystem. $P(\Delta)$ then measures the probability that a cumulative value of δ_i 's as large as the one observed is obtained by chance. In this work, we run 2,500 randomizations for each cluster and consider that all clusters for which $P(\Delta) \geq 0.1$ pass the DS test. The fractions ($P(\Delta)$ values) of the clusters that pass both this test and the virialization test are shown in Table 3.

4. Results

4.1. Properties of the subset of most dynamically relaxed clusters

Fourteen of the 37 cluster regions in the final dataset pass the two tests of virialization and substructure. The subset of these systems, which are expected to constitute the most dynamically relaxed clusters among the evolved galaxy aggregations included in our final cluster sample, will be hereafter referred as the maximally relaxed (MR) cluster sample. The main properties of these 14 cluster regions are listed in Table 1.

All clusters in the MR sample possess virial radii larger than 1 Mpc, with a mean value of 1.47 Mpc. The virial masses are on the order of $10^{14} M_{\odot}$, with an average of $4.12 \cdot 10^{14} M_{\odot}$. Cluster velocity dispersions range from about 500 km s^{-1} for the lower mass clusters up to almost 900 km s^{-1} for the most massive systems. The total number of galaxies in this cluster sample is 1486, consisting of 387 S0s and 1099 galaxies of other morphological types. The

activity distribution within the S0 population is as follows: 320 galaxies (83%) are S0-PS, 52 (13%) are S0-AC, and 15 (4%) are S0-TR. These figures are consistent with the findings reported by Tous et al. (2020) and Jiménez-Palau et al. (2022), who noted that active lenticulars (i.e., the AC+TR classes) tend to avoid high-density regions.

In Appendix A, we present plots showing the projected phase space of the MR cluster regions up to $3 R_{\text{vir}}$, as well as the corresponding sky distributions that provide visual aids to determine how closely the spatial locations of the BCGs align with the clusters' central coordinates and the peaks of X-ray emission.

4.2. BCG classification of the clusters in the MR sample

Table 2 lists the absolute magnitude, magnitude gaps, and velocities of the BCGs of the MR cluster regions, together with the BCG status of the clusters. This Table also includes the intercentric distances d_{BCG} and d_{Xray} which are, respectively, the projected distances from the BCGs to the center of the galaxy distribution and to the peak of X-ray emission.

When looking at the magnitude gaps between the two brightest galaxies, we see that in most of the MR clusters they are larger than 0.45, making them single-BCG systems. However, there are two systems in the MR sample with a double-BCG and three others that, according to the classification scheme defined in Section 3.4, have been considered non-BCG systems. Two of these non-BCG systems also show relatively low values of $P(\Delta)$, implying that small magnitude gaps between the brightest galaxies in a cluster tend to be associated with the presence of substructure.

The projected distances between BCGs and both the centers of the galaxy distributions and the peaks of X-ray emission are generally small compared to the virial radii of their host clusters. However, in the four galaxy aggregations where $\Delta M_{2-1} < 0.45$, this is not the case, reinforcing the idea that the BCGs identified in these systems are not truly dominant objects.

In the special case of cluster 2236, where there are two prominent BCGs separated by only 0.005 mag, both galaxies pass, however, the indicator test, with Z -scores of -0.27 and -0.17 for the first and second brightest galaxies, respectively. Additionally, the sky location of the slightly fainter of the two BCGs coincides well with that of the peak of X-ray emission, whereas the other BCG lies further from the cluster and X-ray centers (see the corresponding plot in Appendix A).

4.3. The projected phase-space distribution of S0s in cluster regions

We have obtained the two-dimensional PPS diagram for the ensemble of the 14 maximally relaxed local clusters. This has been achieved by plotting in a single chart the projected radii of all galaxies included in the MR cluster sample against their LOS velocities. To ensure consistent treatment of all cluster galaxies, their projected cluster-centric radii are normalized by the virial radii of their parent clusters, whereas their recession velocities are expressed in units of their own clusters' velocity dispersion. Common

T-ID	A-ID	N_{gal}	z_{clu}	RA [deg]	Dec [deg]	R_{vir} [Mpc]	M_{vir} [$10^{14}M_{\odot}$]	σ_{clu} [km/s]
205	A1691	133	0.073	197.8042	39.2410	1.9240	8.2941	877.61
262	A1809	104	0.080	208.2826	5.1494	1.6302	5.0458	751.00
292	A1904	168	0.072	215.5512	48.5482	1.7890	6.6678	814.73
571	A1663	129	0.084	195.6563	-2.4993	1.7826	6.5964	826.23
734	A2028	103	0.077	227.3734	7.5756	1.5581	4.4052	715.59
804	-	41	0.073	232.3093	52.8827	1.1058	1.5749	504.66
2236	-	69	0.063	208.0137	46.3524	1.2163	2.0955	547.36
2316	-	44	0.072	163.5068	54.8142	1.1367	1.7104	518.04
2496	A1913	108	0.054	216.6968	16.6641	1.1615	1.8248	516.35
2620	-	96	0.039	233.1474	4.6955	1.1647	1.8402	506.75
5183	A1377	96	0.052	176.8621	55.7434	1.6125	4.8827	713.87
5567	-	109	0.045	230.4534	7.6990	1.4521	3.5656	636.96
5905	A1185	150	0.032	167.7492	28.6817	1.3149	2.6477	566.50
8062	A1314	136	0.033	173.7296	49.0778	1.7707	6.4650	764.11
mean:	-	106	0.061	-	-	1.4728	4.1154	661.42

Table 1: Sample of the 14 most relaxed clusters (MR sample), that are used for the phase-space study of S0 galaxies. The first two columns denote the group id assigned by Tempel et al. (2017), and for clusters identified as Abell clusters the Abell id, respectively. The last row of the table shows the mean column value when appropriate.

T-ID	M_{BCG} [mag]	$\Delta\mathcal{M}_{2-1}$ [mag]	$\Delta\mathcal{M}_{3-2}$ [mag]	BCG-status	v_{BCG} [km/s]	d_{BCG} [Mpc]	d_{Xray} [Mpc]
205	-23.169	0.525	0.790	single	-35.99	0.128	0.167
262	-23.213	0.980	0.348	single	-176.69	0.036	0.133
292	-23.024	0.900	0.342	single	-208.25	0.132	0.390
571	-21.836	0.169	0.077	no BCG	-129.18	0.483	0.479
734	-22.867	1.231	0.234	single	72.36	0.431	0.385
804	-23.052	1.581	0.254	single	-159.77	0.106	0.296
2236A	-22.585	0.005	0.995	double	-153.01	0.706	1.104
2236B	-22.579	-0.005	0.995	double	-94.18	0.413	0.072
2316	-22.107	0.621	0.084	single	-23.24	0.644	0.238
2496	-21.919	0.320	0.022	no BCG	-2.91	0.166	0.081
2620	-22.249	1.242	0.041	single	9.27	0.060	0.286
5183	-22.684	0.387	0.716	double	-42.23	0.105	0.177
5567	-22.492	1.058	0.368	single	-166.14	0.055	0.003
5905	-21.800	0.441	0.070	no BCG	119.58	0.347	0.445
8062	-22.271	0.552	0.623	single	56.09	0.062	0.037
mean:	-22.519	0.715	0.355	-	-60.01	0.247	0.302

Table 2: Properties of the BCGs in the 14 clusters included in the MR sample. The first column shows the cluster id of Tempel et al. (same as in Table 1). The last two columns provide the distance between the BCGs and the cluster centers, as well as the distance between BCGs and the peak of X-ray emission, respectively. The last row of the table shows the mean column value when appropriate.

caustic lines up to three virial radii⁵ are then constructed from the mean mass of the virialized cluster cores of the ensemble, assuming a NFW density profile with $C = 6$. Figure 1 shows the PPS distribution of the ensemble, distinguishing between lenticular galaxies and other morphological types, while splitting the population of S0s according to their spectral (activity) classes (S0-PS, S0-AC, S0-TR). The two insets in Figure 1 highlight the significant differences shown by the distributions of the passive, PS (left), and active, AC and TR (right), lenticulars in the PPS diagram, especially towards the clusters core.

Further evidence of the important differences characterizing the various spectral types of S0s is provided in Figure 2, which depicts the Gaussian kernel density estimates of the projected radius (upper panel) and the absolute LOS velocity (lower panel) for each spectral subpopulation of

⁵ This is the distance up to which member galaxies have been included in each of the individual clusters.

S0s. This figure shows that passive lenticulars (S0-PS) are more concentrated towards smaller radii and have a smaller absolute velocity dispersion, whereas active systems (S0-AC and S0-TR) exhibit peaks of these distributions at greater radii and larger absolute velocities. Active S0s also show weaker and broader peaks than their passive counterparts, particularly in the distribution of projected radii. Additionally, all subpopulations display prominent tails extending towards larger values, that again are more noticeable in the radial coordinate. These tails suggest a hint of a secondary peak in the outermost cluster regions that we suspect could be related with the backsplash radius of clusters (see, e.g. Mamon et al. 2004).

Cluster galaxies can also be categorized by their tenure as cluster members. Following the approach of Rhee et al. (2017), we divided the PPS diagram into several regions based on the typical time since a galaxy’s infall (see their Figure 6). In Figure 1, the original five regions defined by Rhee et al. have been consolidated into three by combin-

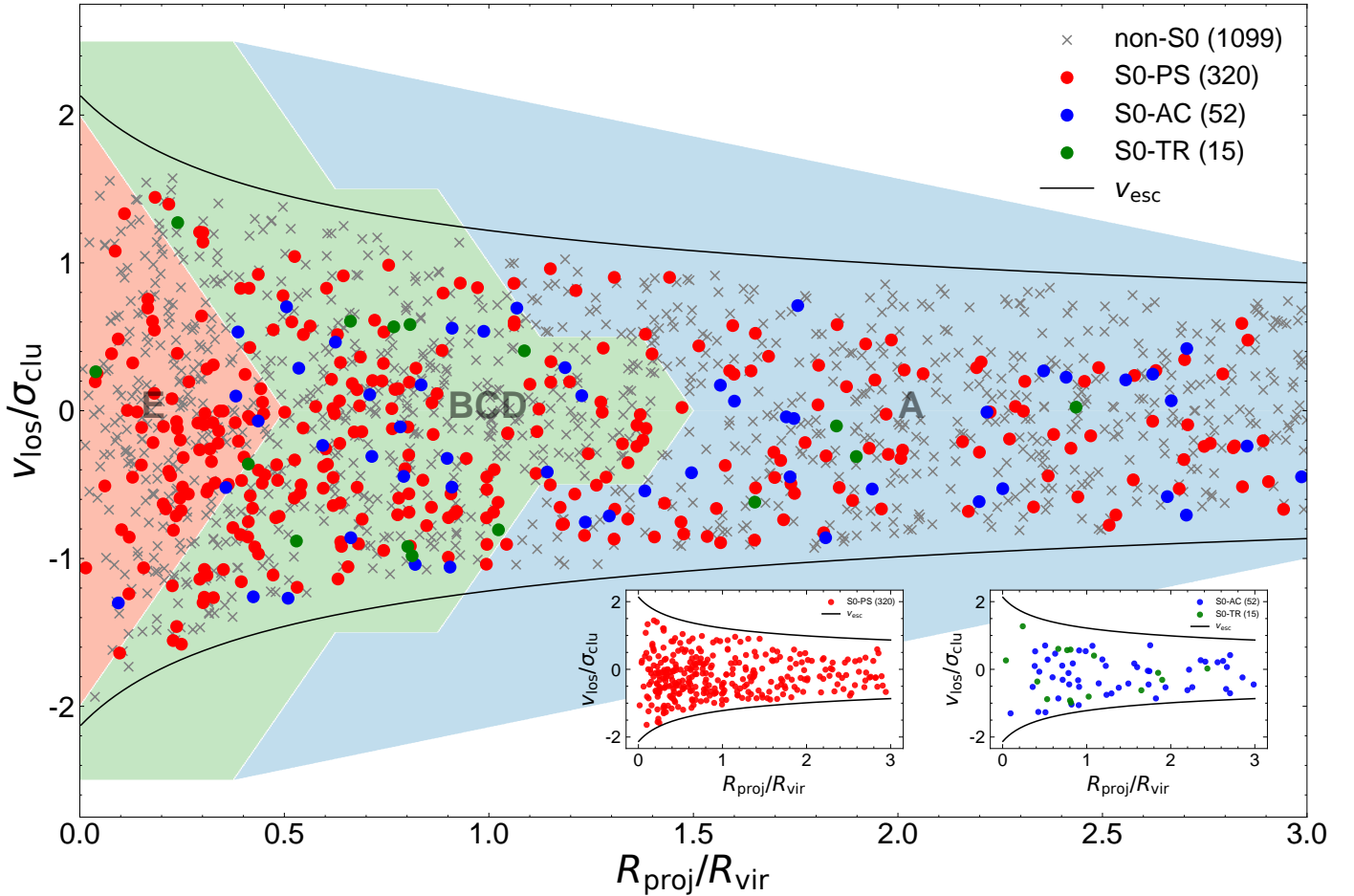


Fig. 1: Projected phase-space diagram of cluster galaxies members of some the most relaxed local clusters (MR sample). All galaxies lie within the black caustic lines. Red filled dots identify S0-PS, blue filled dots S0-AC, and green filled dots S0-TR, whereas grey crosses are used for the rest of morphologies. The projected radii of galaxies are normalized by the mean virial radius, and their LOS velocities by the mean velocity dispersion of their parent clusters. The semitransparent colored regions delineate the infall regions from Rhee et al. (2017). To facilitate the visualization of the differences in the distributions of active and passive S0s, the two inset panels display exclusively the PPS distributions of the passive (left inset) and active (right inset) objects, with S0-TR counted as active lenticulars.

ing the intermediate regions B, C, and D into a single area named BCD. This is done to ensure that all infall regions contain a sufficiently large number of active lenticulars. Galaxies in the most distant region A are short-term cluster members still in the infalling process, while objects in the intermediate region BCD—most of them already within $1 R_{\text{vir}}$ —were likely accreted earlier, and galaxies in the central region E are the oldest cluster members. To enhance our understanding of their PPS distribution and assess differences in cluster membership between active and passive systems, we have computed the fractional distribution of the three spectral S0 classes within each of these three main infall areas of the PPS (see Figure 4), with the 1σ errors of the different fractions estimated from 1000 bootstrap resamples of the S0 distributions in each one of the infall regions.

Although the red, passive lenticulars are by far the dominant spectral type in every infall regime of the PPS, their fractional abundance systematically increases towards the cluster core, whereas the opposite is true for S0-AC lenticulars, which show a monotonic decline in their relative fraction between the outskirts and the innermost cluster re-

gions. For their part, the S0-TR show an undefined behavior, probably due to their limited contribution to the total S0 sample, which adds significant uncertainty to any statistical measurement that we want to infer from this subset.

Using this division of the PPS into different infall regions, we have estimated the typical times since infall into the cluster for the different S0 spectral classes. This was done by multiplying the fraction of each spectral class in each region by the mean time since infall assigned to that region (Oh et al. 2019), which is 0.44 Gyr for region A, 3.52 Gyr for region BCD, and 5.82 Gyr for region E. With this approach, the average times since infall are 2.98 Gyr for S0-PS, 2.05 Gyr for S0-AC, and 2.75 Gyr for S0-TR. The most remarkable aspect of these numbers is the clear difference of almost 1 Gyr in the length of membership between the passive and active S0s, indicating that quiescent lenticular galaxies have been part of clusters significantly longer than their active counterparts. It is also notable that the mean cluster membership time of the S0-AC subpopulation doubles the typical timescale for disk gas removal through RPS, which is about 1 Gyr (e.g. Lotz et al. 2019). This discrepancy alone suggests that active S0s are unlikely to be the

T-ID	Z-score	$P(\Delta)$
205	-0.04 (-0.24, 0.28)	0.71
262	-0.23 (0.32, -0.38)	0.18
292	-0.25 (-0.32, 0.32)	0.39
571	-0.15 (-0.31, 0.37)	0.11
734	0.10 (-0.38, 0.38)	0.97
804	-0.31 (-0.34, 0.48)	0.96
2236A	-0.27 (-0.43, 0.41)	0.92
2236B	-0.17 (-0.43, 0.41)	0.92
2316	-0.04 (-0.57, 0.36)	0.74
2496	-0.01 (-0.28, 0.26)	0.84
2620	0.02 (-0.44, 0.25)	0.32
5183	-0.06 (-0.33, 0.34)	0.41
5567	-0.26 (-0.29, 0.30)	0.83
5905	0.21 (-0.28, 0.36)	0.20
8062	0.07 (-0.24, 0.17)	0.26
mean:	-0.09 (-0.34, 0.33)	0.57

Table 3: Results of the indicator test as well as the test of substructure for the 14 most relaxed clusters that pass both of them. The cluster 2236 has two entries (A,B) with different Z-scores, due to the presence of two dominant galaxies of nearly identical luminosity (see Table 2), which therefore requires them both to pass the indicator test. The last row of the table shows the mean column values.

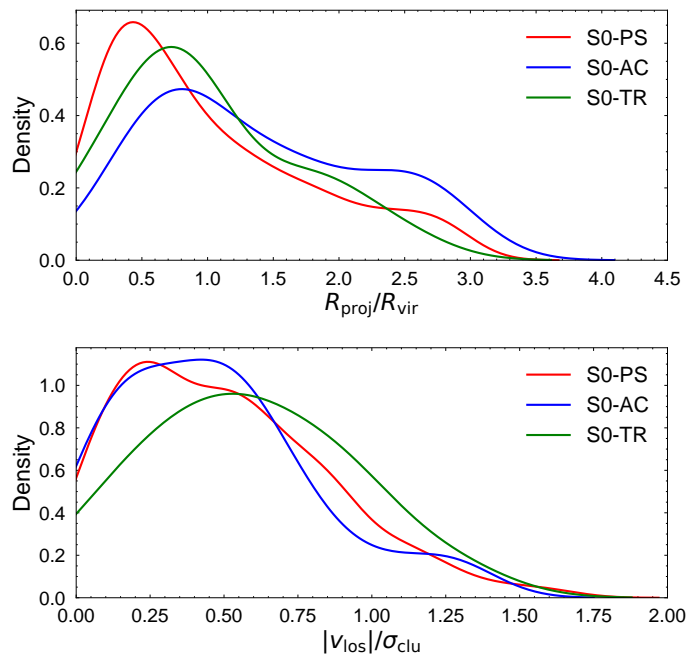


Fig. 2: Kernel density estimations for the radial and velocity dispersion components of the PPS distributions of the three spectral classes of S0 galaxies in the MR cluster sample. The red solid curves are for S0-PS, the blue for S0-AC, and the green for S0-TR galaxies.

final stage of fading spirals as suggested by some authors (see also e.g. Rathore et al. 2022 and Sec. 5) as long as star formation quenching precedes morphological transition.

To further investigate the different distributions of active and passive lenticulars in the PPS of clusters, we performed two-dimensional Kolmogorov-Smirnov (2D-KS) tests to compare the distributions in this subspace of the three spectral type populations with each other and with

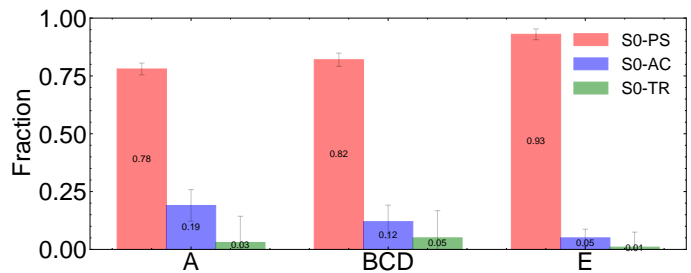


Fig. 3: The fractions of S0 spectral types in the PPS infall regions defined in Figure 1 are shown. Red bars represent S0-PS, blue bars represent S0-AC, and green bars represent S0-TR galaxies. The 1σ error bars have been calculated from 1000 bootstrap resamples with replacement of the original distributions in each region.

Sample 1	Sample 2	p -value
S0	others	0.0145
S0-PS	S0-AC	0.0338
S0-PS	S0-TR	0.308
S0-AC	S0-TR	0.146
Q	MS	0.0287
Q	GV	0.0278
MS	GV	0.522

Table 4: Results of the 2D-KS tests for the different spectral and Δ MS classes. The first two columns list the subsets that are compared, while the last column shows the two-sided p -value of the KS test.

the entire sample of cluster galaxies. The public code NDTEST⁶ was used for this analysis. Similar to previous statistical tests, a two-sided p -value less than 0.10 is taken as an indication of a significant difference between the samples involved.

When comparing the population of S0s with all other cluster galaxies in the PPS, the two-tailed p -value of the 2D-KS test is 0.0145. This indicates a highly significant difference in the distributions, attributable to the well-known fact that S0 galaxies are more concentrated towards the cluster cores compared to other Hubble types. Additionally, the 2D-KS test between S0-PS and S0-AC yields a p -value of 0.0338, indicating that the distributions of these two subpopulations in the PPS are also significantly different (see Figure 1). In contrast, the comparisons between S0-AC and S0-TR, as well as between S0-PS and S0-TR yield larger p -values of 0.146 and 0.308, respectively. This is consistent with the fact that the S0-TR galaxies share similarities with both passive and active systems due to their intermediate location in the PC1-PC2 diagram. Nevertheless, we remind the reader that the results concerning this latter spectral class must be interpreted with caution, due to the small number of S0-TR galaxies. The outcomes of all the 2D-KS tests performed are listed in Table 4.

Insights into the evolution of S0 galaxies in clusters can also be derived by measuring a quantity intimately related to the SF process: the specific star-formation rate (SSFR). To implement this approach, we have defined a "distance" Δ MS for our cluster S0s relative to the Main Sequence of star-forming galaxies (Renzini & Jie Peng 2015) from the

⁶ Written by Zhaozhou Li, <https://github.com/syrte/ndtest>

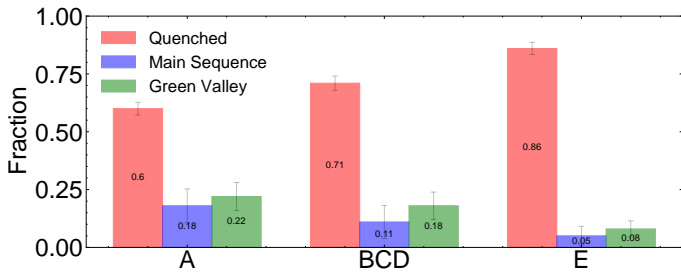


Fig. 4: As Fig. but for the ΔMS types. In this plot red bars represent S0-Q, blue bars S0-MS, and green bars S0-GV galaxies.

following equation:

$$\Delta MS = \log \left[\frac{\text{SFR}}{M_{\odot} \text{ yr}^{-1}} \right] - 0.76 \log \left[\frac{M_{\star}}{M_{\odot}} \right] + 7.6, \quad (14)$$

where for the star-formation rates (SFR) and stellar masses of the galaxies (M_{\star}), we use the values inferred by Salim et al. (2016) from the observed spectral energy distribution of these objects across the IR to UV electromagnetic domains. Then, following Tous et al. (2023), we classify S0 galaxies into Main Sequence (MS) objects if they have $\Delta MS \geq -0.5$, Green Valley (GV) objects if $-0.5 \leq \Delta MS \leq -1.1$, and Quenched (Q) objects when $\Delta MS \leq -1.1$. Among the total 387 S0 galaxies in the MR sample, 272 objects (70%) are classified as S0-Q, 47 (12%) as S0-MS, and 68 (18%) as S0-GV.

Figure 4 shows the fractions of ΔMS classes in each PPS region, computed in the same fashion as the ones in Figure 4. This new classification produces both fractional abundances and behaviors similar to those obtained from the commensurate spectral classes. Specifically, there is a slight increase in passive/quenched systems in the older cluster regions, while the classes with some degree of star formation (S0-MS and GV) exhibit the opposite trend. Note that due to the large difference in the fractions between quiescent active galaxies, the relative increase of the active systems is significantly higher than the relative decrease experience by passive S0s between the central and outer regions. This further highlights the distinct distributions of active and passive S0s in the PPS of clusters.

As expected, the mean times since infall by region and the outcomes of the 2D-KS tests comparing the PSS distributions for the different ΔMS classes, are fully consistent with those obtained from their corresponding spectral classes. Following the same methodology as before, we find that the S0-Q have typical infall times of 3.18 Gyr, S0-MS of 2.20 Gyr, and S0-GV of 2.40 Gyr. Again, a gap of about 1 Gyr separates the times since infall of the most active and most passive subgroups. For their part, the series of 2D-KS tests yield a low p -value of 0.0287 for the comparison of the distributions of S0-Q and S0-MS galaxies in the latent PPS, while confirming the similarity of the distributions of GV and MS lenticulars with a p -value of 0.522. As with the spectral classes, the results of the 2D-KS tests for the star-forming classes are detailed in Table 4.

4.4. Radial velocity dispersion and SSFR profiles

In this section, we analyze the kinematics and SSFRs of active and passive S0s from their respective projected radial

profiles. To construct these profiles we follow the method described in Bilton & Pimblet(2018; see also references therein), which involves producing continuous radial profiles by weighting the contribution of each galaxy at the projected radius R with a moving Gaussian window function:

$$w_{ij}(R/R_{\text{vir},j}) = \frac{1}{\sigma_R} \exp \left\{ -\frac{(R - R_{ij})^2 / R_{\text{vir},j}^2}{2\sigma_R^2} \right\}, \quad (15)$$

with σ_R the kernel width and R_{ij} the projected radial coordinate of the i -th galaxy of the j -th cluster. The window function w_{ij} is then applied to the variable of interest to get a smooth profile. The kinematics is analyzed from the perspective of LOS velocity dispersion profile:

$$\sigma_{\text{los}}(R/R_{\text{vir}}) = \sqrt{\frac{\sum_{ij} w_{ij}(R/R_{\text{vir},j})(v_{\text{los},i} - \bar{v}_{\text{los},j})^2}{\sum_{ij} w_{ij}(R/R_{\text{vir},j})}}, \quad (16)$$

where $v_{\text{los},ij}$ represents the l.o.s. radial velocity of the i -th galaxy of the j -th cluster and $\bar{v}_{\text{los},j}$ the mean recession velocity of the parent cluster, while the SSFR profile is simply given by

$$SSFR(R/R_{\text{vir}}) = \frac{\sum_{ij} w_{ij}(R/R_{\text{vir},j}) SSFR_{ij}}{\sum_{ij} w_{ij}(R)}, \quad (17)$$

with $SSFR_{ij}$ the individual values for the i -th galaxy of the j -th cluster. In both equations the projected clustercentric distance is expressed in units of R_{vir} .

By calculating the radial profiles in this manner we ensure smooth curves for small sample sizes, which is why we have chosen this method over the classical radial binning. The choice of the kernel width is essential to avoid largely fluctuating profiles for too small windows, or over-smoothing physically relevant features when the windows are too large. In the present case, a common kernel width equal to $0.4 R_{\text{vir}}$ was chosen for all calculations. Besides, to ensure resultant profiles that are not specious, we have combined the small subset of S0-TR galaxies (15 objects), with the 52 S0-AC into a single S0-AC+TR subset of non-passive galaxies.

Figure 5 displays the normalized velocity dispersion profiles of active and passive S0s in the top panel and their SSFR profiles in the bottom panel. Given the observed marked difference in the typical times since infall (see Section 4.3) it is somewhat surprising that the velocity profiles of both active and passive S0s are so much alike, suggesting a common origin for both subpopulations. The clear decline in projected velocity dispersion with clustercentric distance may indicate that clustered S0 galaxies tend to globally fall on radially anisotropic orbits, regardless of their activity level (see the next section for a more detailed discussion). In contrast, the bottom panel reveals a completely different story, with distinctly different SSFR behaviors for active and passive S0s, consistent with expectations. Passive S0s exhibit a nearly flat, featureless radial distribution, centered on very low SSFR values — the mean SSFR of the S0-PS is $3.54 \cdot 10^{-12} \text{ yr}^{-1}$ — that show extremely small $1-\sigma$ errors that are barely distinguishable from the central curve. The profile flatness, its normalization, and minimal variance indicate that the S0-PS are essentially completely quiescent systems. The active S0s, on the other hand, exhibit a rapidly declining SSFR profile from a peak value at

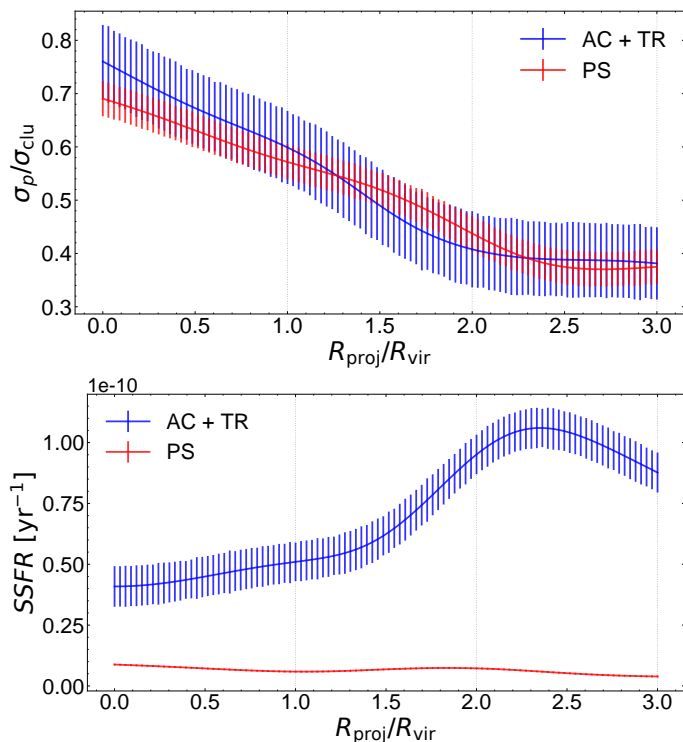


Fig. 5: Projected radial profiles for AC+TR (blue) and PS (red) lenticulars, smoothed with a Gaussian kernel window of $0.4 R_{vir}$. *Top panel*: LOS velocity dispersion profiles of cluster S0s, normalized by the velocity dispersion of their parent cluster. *Bottom panel*: SSFR profiles. In both panels, the projected radius on the horizontal axis is normalized by the virial radius of the host clusters. The vertical dotted gray lines mark the projected distance in steps of the virial radius. Colored bars represent the 1σ errors from 1000 bootstrap resamples with replacement.

$\sim 2.5 R_{vir}$ of $3.82 \cdot 10^{-10} yr^{-1}$, fully comparable with the SSFR of Main Sequence spirals. This decline becomes more gradual around $1.5 R_{vir}$ and continues at the same rate until the cluster center, providing evidence for a two-phase "rapid-then-slow" quenching process. The mean SSFR in cluster regions for the S0-AC+TR subset is $5.74 \cdot 10^{-11} yr^{-1}$.

5. Discussion

Our analysis of the distributions of the active and passive subpopulations of lenticular galaxies in the PPS of local relaxed galaxy clusters has revealed very significant differences, as well as corresponding variations in mean estimated cluster infall times. Our findings indicate that star-forming S0s are younger cluster members, preferentially located in the outer regions of clusters. In contrast, passive S0s have been accreted about 1 Gyr earlier on average and, while dominating the fractional abundances throughout, tend to concentrate closer to the cluster centers (see Fig. 1).

Although the differences between the various spectral types of S0s in the PPS diagram are clear, the most surprising result of our study — which at first glance seems somewhat inconsistent with the above findings — is the striking similarity shown by their radial velocity dispersion profiles (upper panel of Figure 5). This suggests that most lenticular galaxies, regardless of their level of SF, share a similar

dynamical history and, therefore, a common origin. Both the star-forming AC and TR spectral classes and the fully passive lenticular galaxies exhibit radially decreasing velocity dispersion profiles⁷ along the LOS up to $\sim 2 R_{vir}$, but the differences between the curves are insignificant. This appears paradoxical considering that older cluster members are expected to exhibit a more isotropic intrinsic velocity distribution than younger ones, which should result in a flat projected velocity dispersion profile, at least within the virialized cluster regions, as some observations corroborate (see, e.g., Solanes et al. 2001). A plausible explanation is that interspersed with the long-term members are a significant number of recently infallen S0-PS. Indeed, our finding that the S0-PS are well distributed throughout the entire PPS of the cluster regions, maintaining high relative abundances ($\geq 60\%$) with respect to the other spectral classes even beyond $1.5 R_{vir}$, suggests that most S0-PS in cluster regions are accreted from the outside, rather than being the result of the morphological transition of spiral galaxies in the dense cluster cores. Given these conditions, the theoretically anticipated flat projected velocity dispersion profile of the oldest and centrally located S0-PS may be disrupted and altered into a radially decreasing profile due to the inclusion of numerous infalling counterparts.

Regarding the SSFR profiles, the picture is clearer. The SFR for S0-PS remains very low and without noticeable changes in its intensity within $3 R_{vir}$, indicating that a significant fraction of S0s are already joining the clusters as entirely passive systems. Furthermore, the AC+TR lenticulars show the expected progressive decline with cluster-centric radius in their combined SSFR profile, although with an intriguing "rapid-then-slow" quenching. It is generally assumed that disk galaxies lose most, if not all, of their gas once they enter the clusters cores. Thus, one would anticipate that the SFR of S0s would not be much reduced in the cluster outskirts until approaching the virial radius. From there, the SFR would progressively decline faster as galaxies fall to the cluster center, where the ICM is densest and peculiar velocities are highest, maximizing the efficiency of hydrodynamic gas-depletion mechanisms like RPS. However, our findings indicate otherwise: star-forming lenticulars already experience a steep decline in their SSFRs at clustercentric distances beyond $2 R_{vir}$, which transition to a more gradual decline around $1.5 R_{vir}$, well before they reach the outer boundary of the virialized region. This behavior can be explained by assuming that the active S0s are lenticulars rejuvenated by minor mergers occurring in groups located at the outer boundaries of cluster regions, where the merger likelihood is high. These mergers lead to a sudden reignition of their SF, causing the SSFR of these galaxies to temporarily reach levels comparable to those of star-forming spiral galaxies. However, due to the limited amount of gas available in S0 galaxies for the production of new stars, this SF burst fades relatively quickly as the gas is exhausted and not replenished (external gas sweeping by RPS is not expected to contribute to this fast decline at such distances from the cluster centers). When the S0s finally cross the cluster virial radius, their temporarily enhanced SSFRs have already diminished to relatively modest levels. At this point, SF likely persists only in the central regions of the galaxies, which are more re-

⁷ A slightly steeper projected velocity dispersion profile is obtained when only S0-AC are considered.

sistant to RPS. Consequently, the reduction of SF in the innermost cluster regions becomes much more gradual, primarily driven by internal secular quenching. The fact that the radial gradient of the SSFR remains essentially constant for $R \lesssim 1.5 R_{\text{vir}}$ suggests that external gas-depletion mechanisms also contribute minimally to the fading in this later stage. On the other hand, lenticular galaxies that do not experience a merger in the cluster outskirts to rejuvenate star formation will simply infall as already fully passive objects.

6. Conclusions

We conclude by summarizing the most important findings from this study:

- Local, relaxed galaxy clusters harbor not only passive, but also actively star-forming lenticular galaxies. However, passive lenticulars dominate the total number of S0s at each and every dynamically relevant location that can be defined within galaxy cluster regions.
- The projected phase space (PPS) distributions of active and passive S0s are significantly different, with active systems preferring the clusters' outskirts and passive systems the innermost regions.
- Active S0s are on average younger cluster members than passive S0s, with a gap in mean membership length of about 1 Gyr.
- Even though passive and active lenticulars have significantly different phase-space distributions and cluster infall times, they show similar, radially anisotropic velocity dispersion profiles. This is considered as an indication that a substantial fraction of passive S0s are not produced in the cluster centers during the virialization of these structures but arrive later to the cluster via secondary infall.
- Passive S0s show a flat radial specific star-formation rate (SSFR) profile, meaning that they join clusters as already quiescent objects. In contrast, active lenticulars show two regimes in their radial SSFR profile, where a drastic decrease between ~ 2.5 and $1.5 R_{\text{vir}}$ is followed by a more gradual inwards decline, providing evidence for a "rapid-then-slow" quenching. This aligns well with a scenario where S0 galaxies are initially rejuvenated through (minor) mergers in groups on the outskirts of clusters, then undergo a relatively rapid decline in their star-formation (SF) rates as their small gas reservoirs are quickly depleted, and finally, as they approach and enter the central cluster region, adopt a more gradual quenching with SF persisting only in their inner disks.

Acknowledgements. I want to thank my advisors of the master's thesis, Prof. Jose Maria Solanes and Dr. Josep Lluís Tous for their constant support and guidance throughout the whole project. Without them this work would not have been possible. Also, I want to express my deepest gratitude to my fellow master students for constantly supplying me with laughter and interesting insights into their various fields of study. Last but not most importantly, I want to dedicate this work to my family and closest friends, as a sign of utmost love and respect for all their sacrifices and contributions to making my life more fulfilling and giving me the motivation to constantly improve.

References

Alam, S., Albareti, F. D., Allende Prieto, C., et al. 2015, ApJS, 219, 12

Barnes, J., Dekel, A., Efstathiou, G., & Frenk, C. S. 1985, ApJ, 295, 368

Beers, T. C., Flynn, K., & Gebhardt, K. 1990, AJ, 100, 32

Beers, T. C., Geller, M. J., & Huchra, J. P. 1982, ApJ, 257, 23

Berrier, J. C., Stewart, K. R., Bullock, J. S., et al. 2009, ApJ, 690, 1292

Bilton, L. E. & Pimblet, K. A. 2018, Monthly Notices of the Royal Astronomical Society, 481, 1507

Bryan, G. L. & Norman, M. L. 1998, ApJ, 495, 80

Cocato, L., Fraser-McKelvie, A., Jaffé, Y. L., et al. 2022, MNRAS, 515, 201

Crowl, H. H. & Kenney, J. D. P. 2008, AJ, 136, 1623

Darriba, L. & Solanes, J. M. 2010, A&A, 516, A7

Deeley, S., Drinkwater, M. J., Sweet, S. M., et al. 2021, MNRAS, 508, 895

Deeley, S., Drinkwater, M. J., Sweet, S. M., et al. 2020, MNRAS, 498, 2372

Diaferio, A. & Geller, M. J. 1997, ApJ, 481, 633

Domínguez Sánchez, H., Bernardi, M., Nikakhtar, F., Margalef-Bentabol, B., & Sheth, R. K. 2020, MNRAS, 495, 2894

Domínguez Sánchez, H., Huertas-Company, M., Bernardi, M., Tuccillo, D., & Fischer, J. L. 2018, Monthly Notices of the Royal Astronomical Society, 476, 3661

D'Onofrio, M., Marziani, P., & Buson, L. 2015, Frontiers in Astronomy and Space Sciences, 2, 4

Dressler, A. 1980, ApJ, 236, 351

Dressler, A., Oemler, Augustus, J., Couch, W. J., et al. 1997, ApJ, 490, 577

Dressler, A. & Shectman, S. A. 1988, AJ, 95, 985

Duarte, M. & Mamon, G. A. 2014, MNRAS, 440, 1763

Eisenstein, D. J., Weinberg, D. H., Agol, E., et al. 2011, AJ, 142, 72

Eliche-Moral, M. C., Rodríguez-Pérez, C., Borlaff, A., Querejeta, M., & Tapia, T. 2018, A&A, 617, A113

Fasano, G., Poggianti, B. M., Couch, W. J., et al. 2000, ApJ, 542, 673

Fraser-McKelvie, A., Aragón-Salamanca, A., Merrifield, M., et al. 2018, MNRAS, 481, 5580

Gebhardt, K. & Beers, T. C. 1991, ApJ, 383, 72

Gunn, J. E. & Gott, J. Richard, I. 1972, ApJ, 176, 1

Halliday, C., Milvang-Jensen, B., Poirier, S., et al. 2004, A&A, 427, 397

Jiménez-Palau, C., Solanes, J. M., Perea, J. D., del Olmo, A., & Tous, J. L. 2022, MNRAS, 515, 3956

Kaviraj, S., Schawinski, K., Devriendt, J. E. G., et al. 2007, ApJS, 173, 619

Koulouridis, E., Clerc, N., Sadibekova, T., et al. 2021, AA, 652, A12

Larson, R. B., Tinsley, B. M., & Caldwell, C. N. 1980, ApJ, 237, 692

Lotz, M., Remus, R.-S., Dolag, K., Biviano, A., & Burkert, A. 2019, MNRAS, 488, 5370

Macciò, A. V., Dutton, A. A., & van den Bosch, F. C. 2008, MNRAS, 391, 1940

Mamon, G. A., Sanchis, T., Salvador-Solé, E., & Solanes, J. M. 2004, A&A, 414, 445

McGee, S. L., Balogh, M. L., Bower, R. G., Font, A. S., & McCarthy, I. G. 2009, MNRAS, 400, 937

Moore, B., Lake, G., Quinn, T., & Stadel, J. 1999, MNRAS, 304, 465

Mosteller, F. & Tukey, J. W. 1977, Data analysis and regression. A second course in statistics

Navarro, J. F., Frenk, C. S., & White, S. D. M. 1995, MNRAS, 275, 56

Nulsen, P. E. J. 1982, MNRAS, 198, 1007

Oh, S., Kim, K., Lee, J. H., et al. 2019, MNRAS, 488, 4169

Pinkney, J., Roettiger, K., Burns, J. O., & Bird, C. M. 1996, ApJS, 104, 1

Pizzardo, M., Geller, M. J., Kenyon, S. J., & Damjanov, I. 2024, A&A, 683, A82

Poggianti, B. M., Fasano, G., Bettoni, D., et al. 2009, ApJ, 697, L137

Querejeta, M., Eliche-Moral, M. C., Tapia, T., et al. 2015, A&A, 579, L2

Quilis, V., Moore, B., & Bower, R. 2000, Science, 288, 1617

Rathore, H., Kumar, K., Mishra, P. K., Wadadekar, Y., & Bait, O. 2022, MNRAS, 513, 389

Renzi, A. & jie Peng, Y. 2015, The Astrophysical Journal Letters, 801, L29

Rhee, J., Smith, R., Choi, H., et al. 2017, ApJ, 843, 128

Rumbaugh, N., Kocevski, D. D., Gal, R. R., et al. 2013, ApJ, 763, 124

Salim, S., Lee, J. C., Janowiecki, S., et al. 2016, ApJS, 227, 2

Solanes, J. M., Manrique, A., García-Gómez, C., et al. 2001, ApJ, 548, 97

Solanes, J. M. & Salvador-Sole, E. 1992, ApJ, 395, 91

- Tapia, T., Eliche-Moral, M. C., Aceves, H., et al. 2017, *A&A*, 604, A105
- Tempel, E., Tuvikene, T., Kipper, R., & Libeskind, N. I. 2017, *A&A*, 602, A100
- Tinsley, B. M. 1980, *Fund. Cosmic Phys.*, 5, 287
- Tiret, O., Combes, F., Angus, G. W., Famaey, B., & Zhao, H. S. 2007, *A&A*, 476, L1
- Tous, J. L., Domínguez-Sánchez, H., Solanes, J. M., & Perea, J. D. 2023, *ApJ*, 942, 48
- Tous, J. L., Solanes, J. M., & Perea, J. D. 2020, *MNRAS*, 495, 4135
- Turner, E. L. & Gott, J. R., I. 1976, *ApJS*, 32, 409
- Wilman, D. J. & Erwin, P. 2012, *ApJ*, 746, 160
- Xiao, M.-Y., Gu, Q.-S., Chen, Y.-M., & Zhou, L. 2016, *ApJ*, 831, 63
- Xu, Weiwei, Ramos-Ceja, Miriam E., Pacaud, Florian, Reiprich, Thomas H., & Erben, Thomas. 2022, *AA*, 658, A59
- Zeldovich, I. B., Einasto, J., & Shandarin, S. F. 1982, *Nature*, 300, 407

Appendix A: Projected phase-space diagrams and sky maps of the most relaxed cluster regions analysed in this study

This appendix presents plots of the two-dimensional PPS diagrams (with absolute LOS velocities) and sky projections for each of the 14 regions identified in this study as containing the most relaxed galaxy clusters at their centers (the MR sample). For each cluster region, the left panel displays the PPS diagram, where the projected radii of the galaxies, normalized by the virial radius of their host clusters, are plotted against their absolute LOS velocities, normalized by the cluster velocity dispersion. The right panel shows the sky positions in right ascension and declination (both in decimal degrees) up to a distance of three virial radii from the cluster center. In all plots, red dots represent the S0-PS, blue dots the S0-AC, and green dots the S0-TR, while the grey crosses denote galaxy members that are non-lenticular. In the PPS diagrams, the black curve depicts the caustic line corresponding to a cluster with a NFW density profile and a total mass equal to the mean virial mass of the systems in the MR sample. In the sky maps, black concentric circles indicate distances of one, two, and three virial radii from the cluster center, which is marked with a black cross, while the peak of X-ray emission is identified with a purple cross, and location of the BCG with an orange cross. If a cluster harbors two BCGs, two orange crosses are drawn. If there is no clear dominant galaxy, no orange cross is shown.

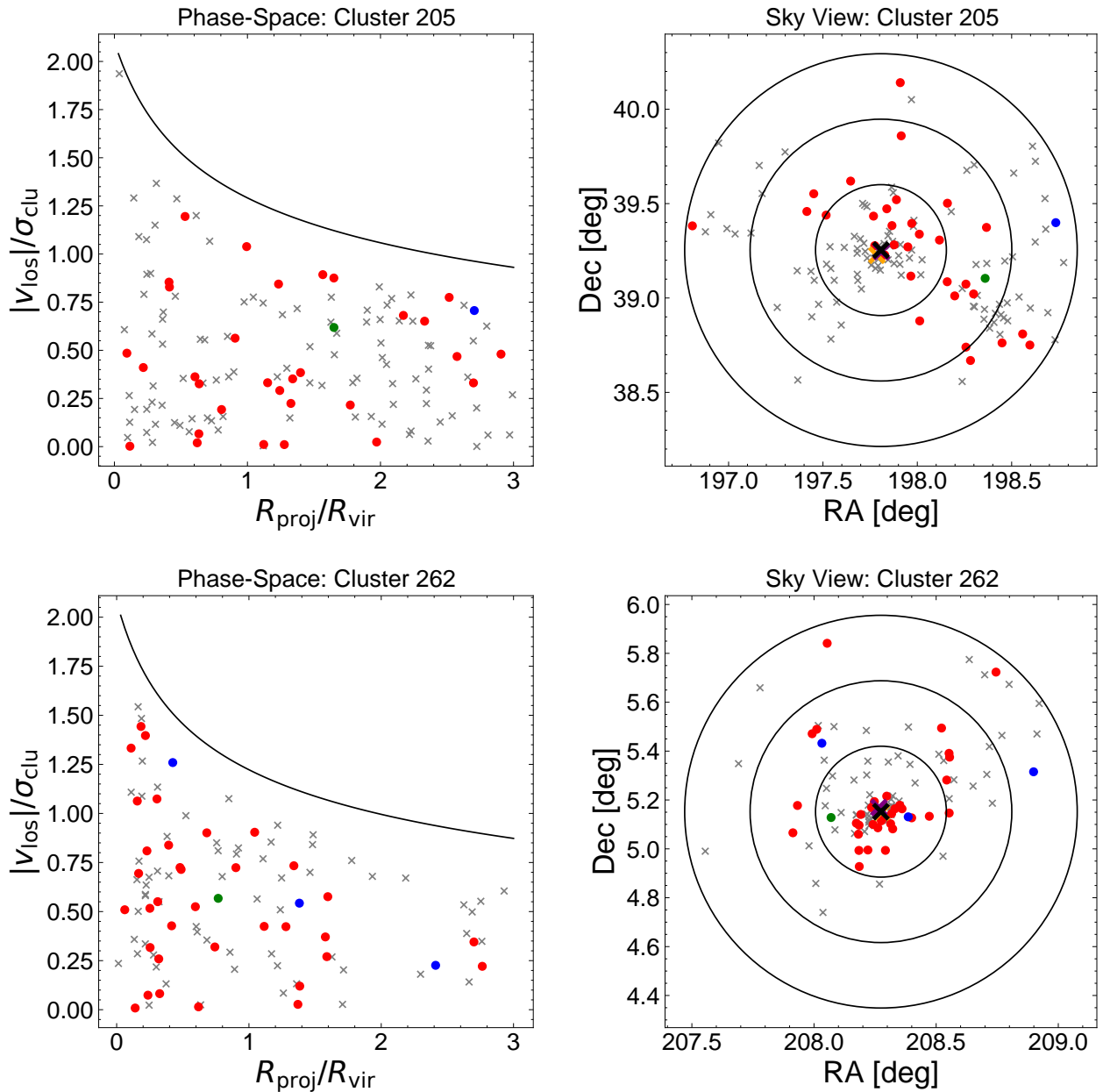


Fig. A.1: Projected phase space (left panels) and sky maps (right panels) of the 14 cluster regions that constitute the MR sample (see the text).

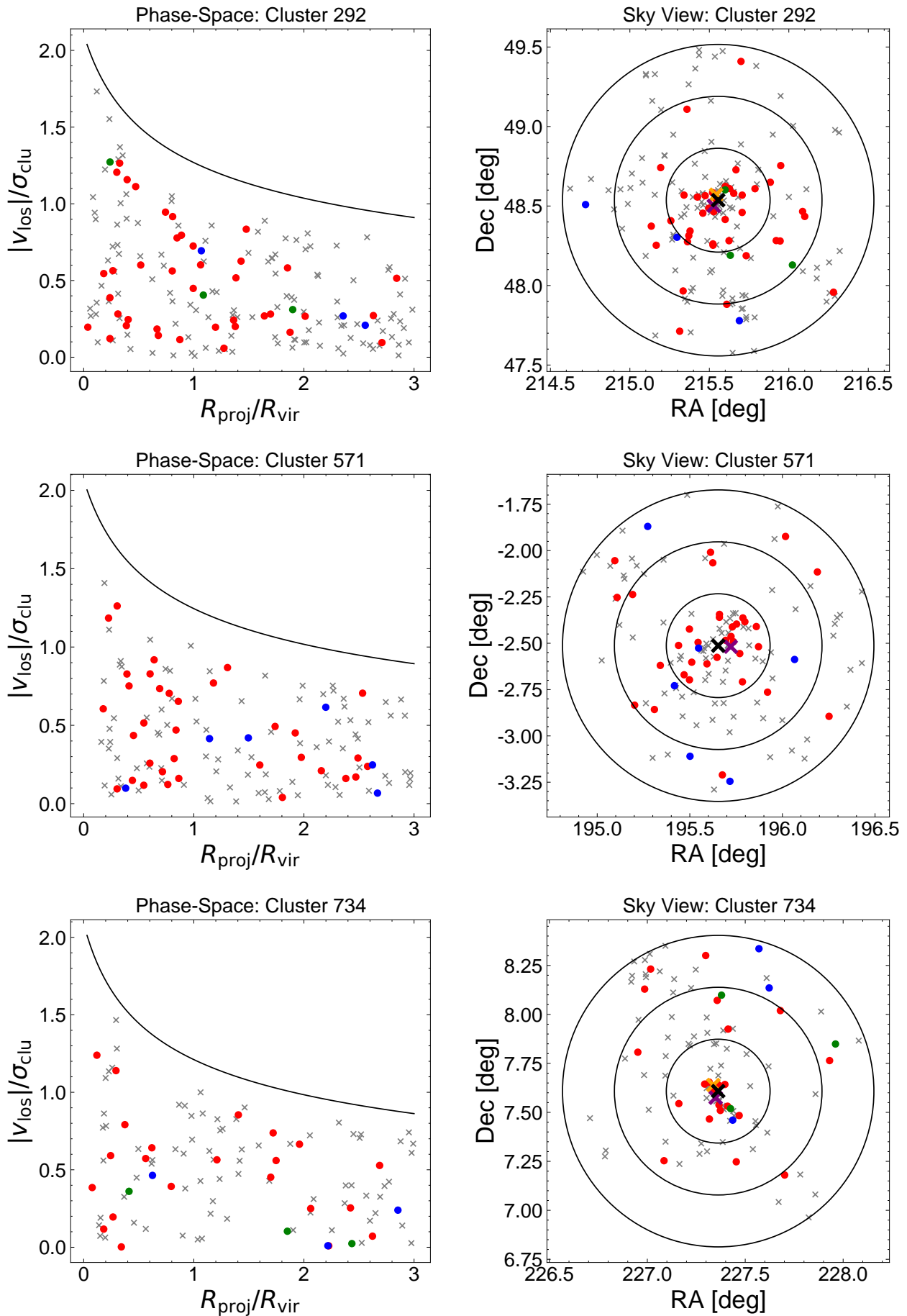


Fig. A.1: - *Continued.*

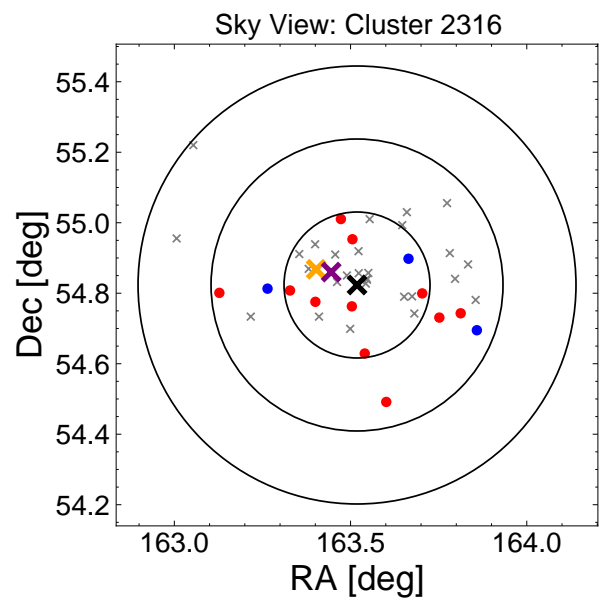
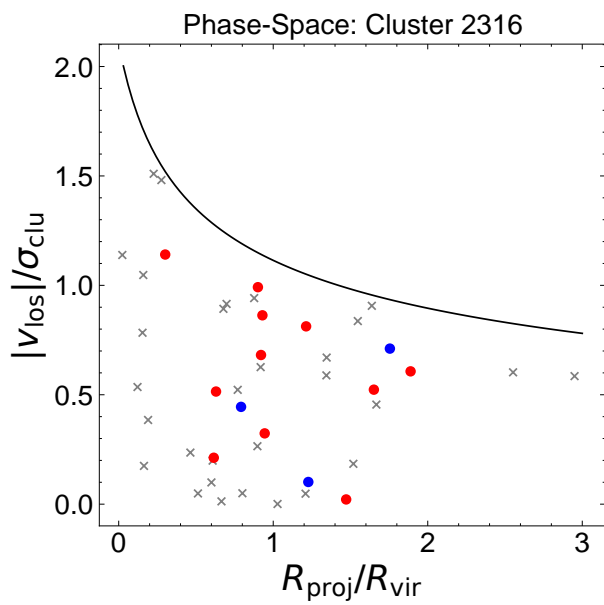
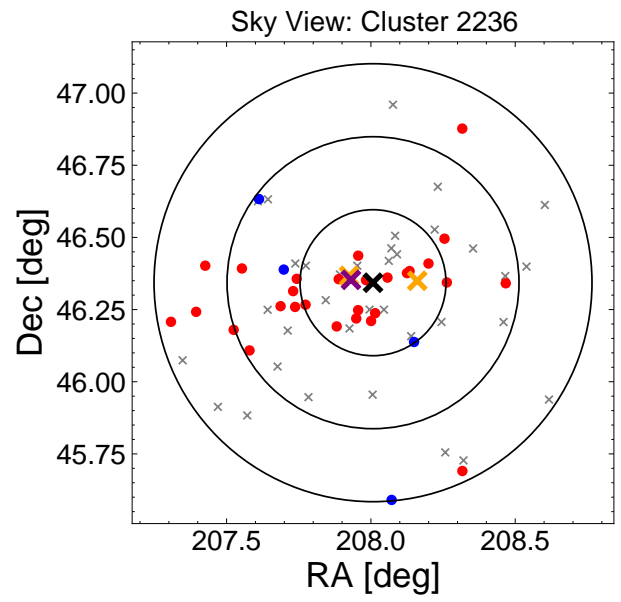
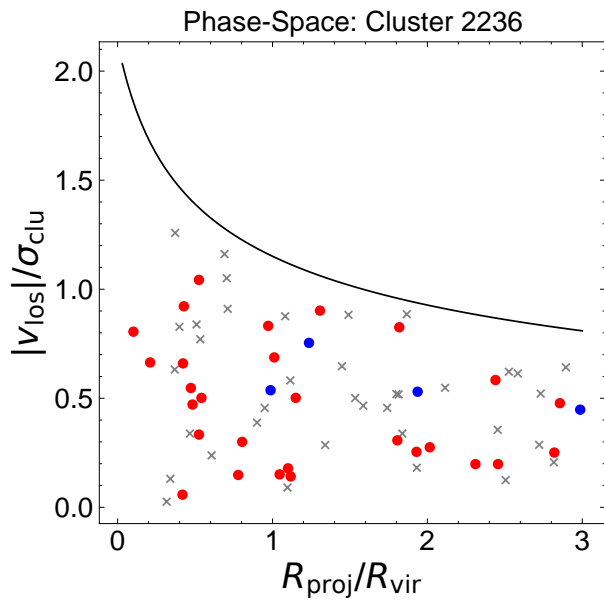
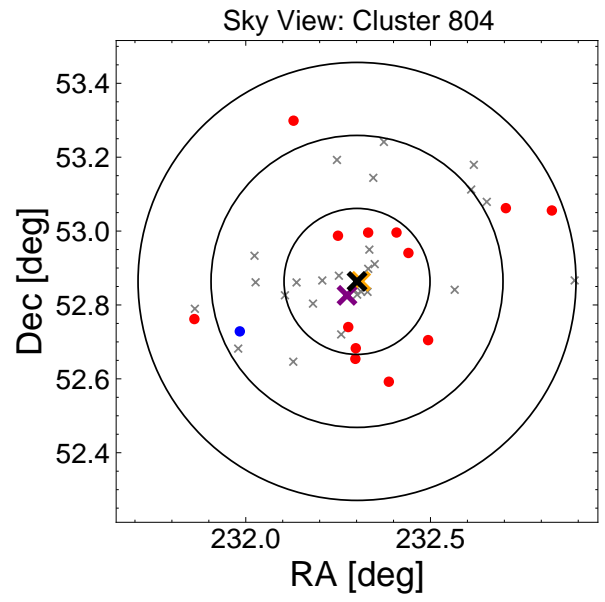
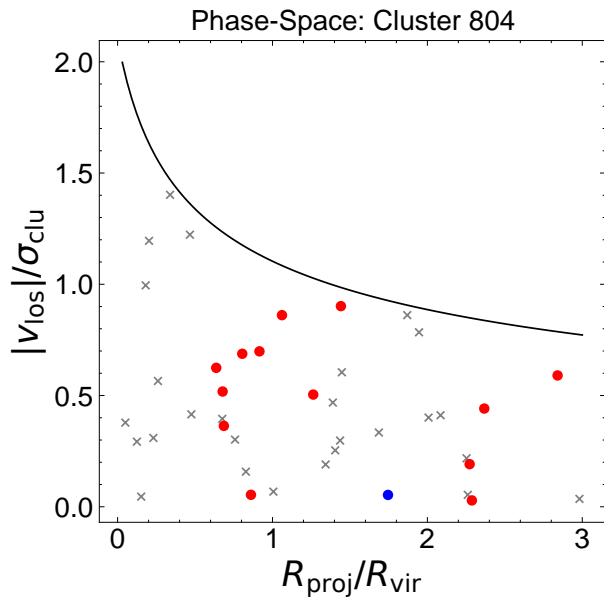


Fig. A.1: - *Continued.*

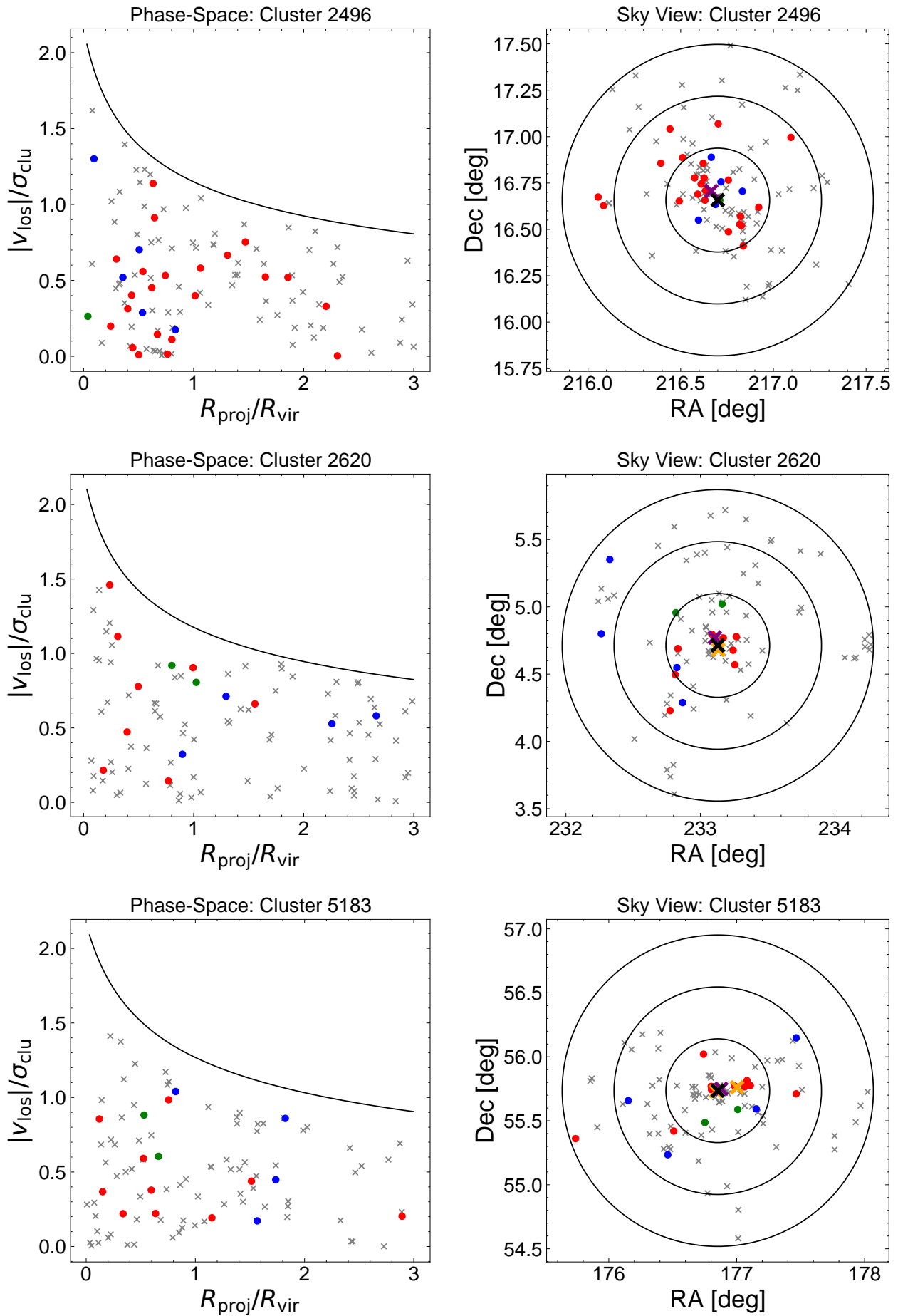


Fig. A.1: - *Continued.*

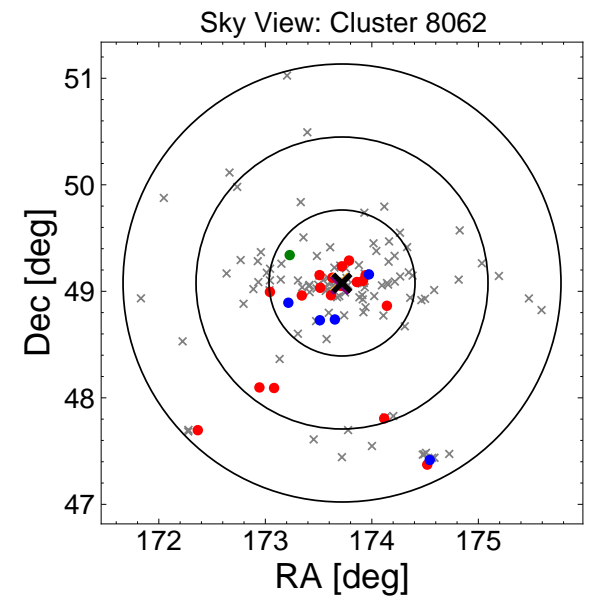
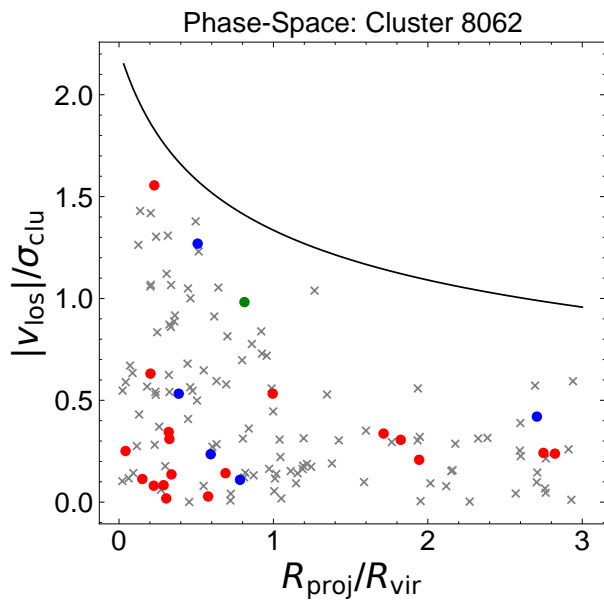
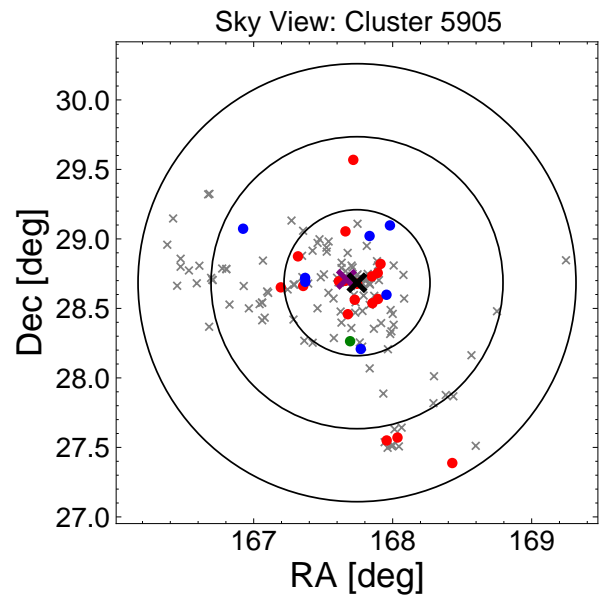
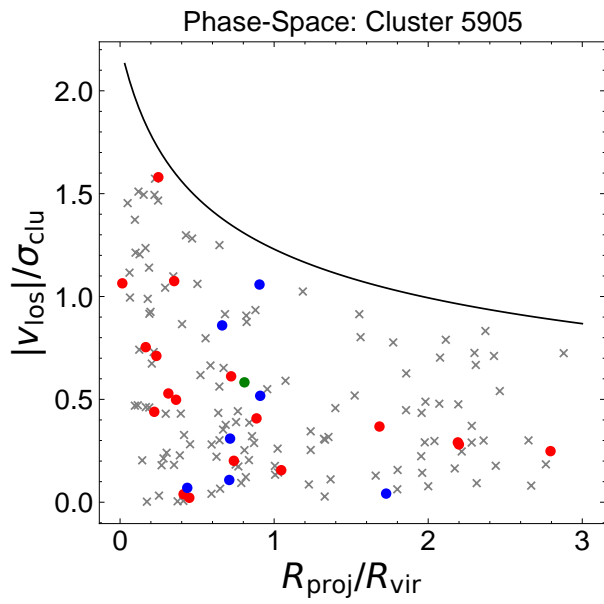
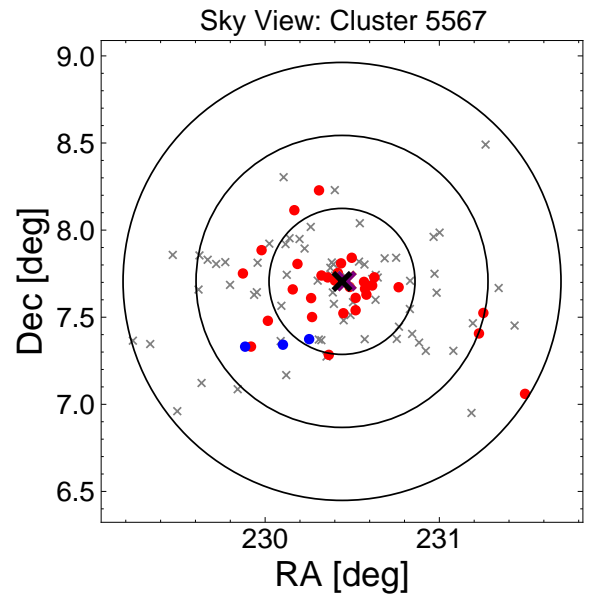
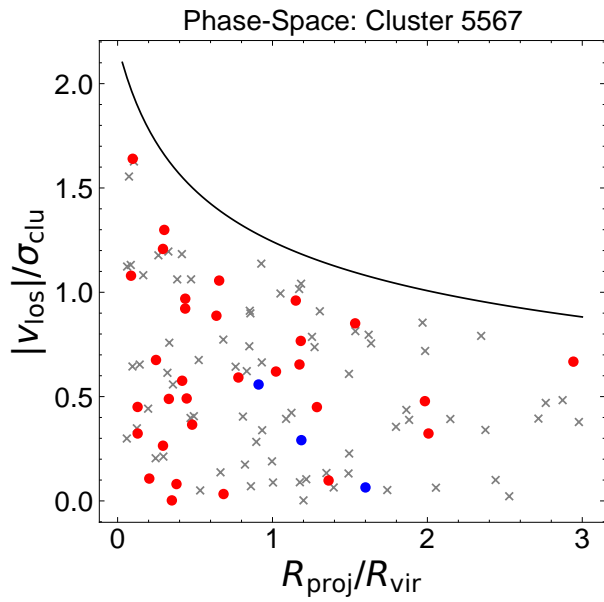


Fig. A.1: - *Continued.*